Journal of Catalysis 279 (2011) 257–268

Contents lists available at ScienceDirect

Journal of Catalysis

journal homepage: www.elsevier.com/locate/jcat

Investigation into the shape selectivity of zeolite catalysts for biomass conversion

Jungho Jae [a], Geoffrey A. Tompsett [a], Andrew J. Foster [b], Karl D. Hammond [a,1], Scott M. Auerbach [a,c], Raul F. Lobo [b], George W. Huber [a,*]

[a] Department of Chemical Engineering, 159 Goessmann Lab., University of Massachusetts, Amherst, MA 01003, United States
[b] Department of Chemical Engineering, University of Delaware, DE 19716, United States
[c] Department of Chemistry, University of Massachusetts, Amherst, MA 01003, United States

ARTICLE INFO

Article history:
Received 4 October 2010
Revised 14 December 2010
Accepted 19 January 2011
Available online 4 March 2011

Keywords:
Zeolite
Pyrolysis
Glucose
Kinetic diameter
Pore size
Shape selectivity

ABSTRACT

We investigate the influence of zeolite pore size and shape selectivity on the conversion of glucose to aromatics. Zeolites having a variety of pore size and shape (small pore ZK-5, SAPO-34, medium pore Ferrierite, ZSM-23, MCM-22, SSZ-20, ZSM-11, ZSM-5, IM-5, TNU-9, and large pore SSZ-55, Beta zeolite, Y zeolite) were synthesized, characterized, and tested in a pyroprobe reactor coupled with GC–MS for the conversion of glucose to aromatics. The aromatic yield was a function of the pore size of the zeolite catalyst. Small pore zeolites did not produce any aromatics with oxygenated products (from pyrolysis of glucose), CO, CO_2 and coke as the major products. Aromatic yields were highest in the medium pore zeolites with pore sizes in the range of 5.2–5.9 Å. High coke yield, low aromatic yields, and low oxygenate yields were observed with large pore zeolites, suggesting that the large pores facilitate the formation of coke. In addition to pore window size, internal pore space and steric hindrance play a major role for aromatic production. Medium pore zeolites with moderate internal pore space and steric hindrance (ZSM-5 and ZSM-11) have the highest aromatic yield and the least amount of coke. The kinetic diameters of the products and reactants were estimated to determine whether the reactions occur inside the pores or at external surface sites for the different zeolite catalysts. This analysis showed that the majority of the aromatic products and the reactants can fit inside the zeolite pores of most of the medium and large pore zeolites. However, in some of the smaller pore zeolites the polycyclic aromatics may form by secondary reactions on the catalyst surface, either directly or via reaction of the smaller aromatics.

1. Introduction

Due to its low cost and abundance, lignocellulosic biomass is being studied worldwide to produce renewable liquid fuels. Fast pyrolysis is a promising route for liquid fuel production from solid biomass [1]. Fast pyrolysis consist of rapidly heating biomass (>500 °C s^{-1}) to intermediate temperatures (400–600 °C) forming pyrolysis vapors. These pyrolysis vapors can then be cooled to make a liquid fuel called a bio-oil or pyrolysis oil [2]. The bio-oils are of low value because they are highly oxygenated and are not compatible with the existing petroleum-derived oils [3]. However, zeolite catalysts can be added to a pyrolysis reactor to convert the pyrolysis vapors directly into aromatics in a process called catalytic fast pyrolysis (CFP) [4–12].

Several researchers have tested zeolite catalysts for the conversion of biomass to aromatics [4–9,11–27]. A range of zeolites have been tested including ZSM-5, Beta zeolite, Y zeolite, Mordenite, silicoaluminophosphate, and several mesoporous materials (Al-MCM-41, Al-MSU-F, and alumina-stabilized ceria MI-575) using a range of different feedstocks including bio-oils, glycerol, sorbitol, glucose, xylose, and biomass feedstocks. In general, these studies showed that the addition of zeolites into the pyrolysis reactor could increase the formation of aromatics. Coke and CO were also formed during this process. The majority of these studies concluded that ZSM-5 was the catalyst that gave the highest yield of aromatics.

Recently, the reaction pathway for the conversion of glucose into aromatics over ZSM-5 has been studied by Carlson et al. as shown in Fig. 1 [28]. This reaction involves chemistry occurring in three phases: within the solid biomass, in the gas phase, and within the catalyst. Glucose first thermally decomposes into anhydrosugars, which are then converted by dehydration reactions into furans. These decompositions can occur homogeneously or on the catalyst. The dehydrated products then enter into the ZSM-5 catalyst where they are converted into aromatics, CO, CO_2, and water through a series of dehydration, decarbonylation, decarboxylation, oligomerization, and dehydrogenation reactions. Coke formation is the major competing reaction with aromatic production.

* Corresponding author. Fax: +1 413 545 1647.
E-mail address: huber@ecs.umass.edu (G.W. Huber).
[1] Present address: Department of Nuclear Engineering, University of California, Berkeley, CA 94720, United States

0021-9517/$ - see front matter © 2011 Elsevier Inc. All rights reserved.
doi:10.1016/j.jcat.2011.01.019

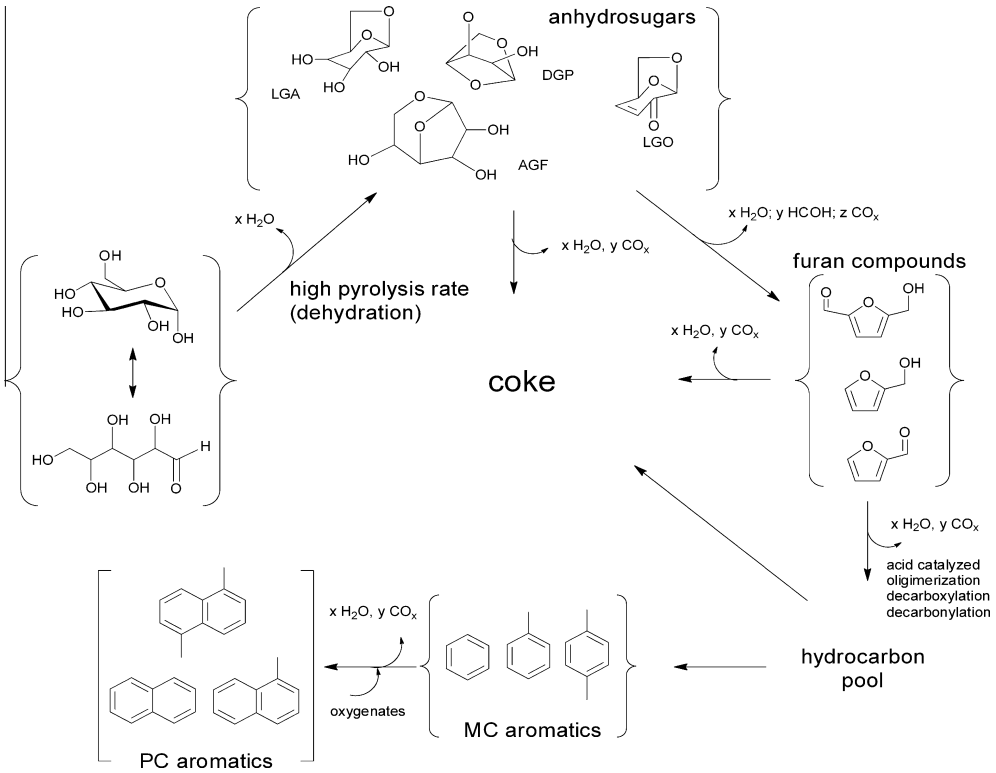

Fig. 1. Reaction chemistry for the catalytic fast pyrolysis of glucose with ZSM-5. Adapted from Carlson et al. [28].

Coke is formed from (1) direct thermal decomposition of glucose; (2) by reactions in the gas phase or (3) by heterogeneously catalyzed reactions.

Zeolites catalyze a wide variety of reactions because of their shape selectivity. Shape selectivity is classically defined as being caused by either mass transfer [29,30] or transition state effects [30–32]. The different pore window size of zeolites ranging from 5 Å to 12 Å cause a mass transfer effect excluding certain reactant molecules based on size relative to the zeolite pore window size. In a similar manner, zeolites limit the formation of products (i.e. high mass-transfer-limited products) larger than the pore size of the zeolite. Shape selectivity is also related to confined spaces within the pores (i.e. pore intersections). Such a confined space restricts certain transition states and influences the course of reaction. Zeolite chemistry can also be further complicated due to reactions on the exterior of the zeolite surface [33,34]. In addition, zeolites can cause a "confinement effect" [35,36] or "solvent effect" [37] where the concentration of different reactants is higher inside the zeolite pores than in the gas phase.

Although previous studies have tested a range of zeolites for biomass conversion, the detailed relationship of the biomass molecular dimensions to zeolite pore size is not well understood. The role of pore size and shape on the catalytic chemistry must be better understood if improved zeolites are to be designed for biomass conversion. The purpose of this paper is to study the influence of zeolite pore size and structure on the conversion of glucose to aromatics by catalytic fast pyrolysis. A range of zeolites, including small pore zeolites (ZK-5 and SAPO-34), medium pore zeolites (Ferrierite, ZSM-23, MCM-22, SSZ-20, ZSM-11, ZSM-5, IM-5, and TNU-9), and large pore zeolites (SSZ-55, Beta zeolite, Y zeolite), were synthesized, characterized, and tested for catalytic fast pyrolysis of glucose. The kinetic diameters for the products and reactants were estimated from properties of the fluid at the critical point to determine whether the reactions occur inside the pores or on the external surface. The constraint index of zeolites is also used to compare the results with the different zeolite catalysts. The results from this paper can be used to help understand whether zeolite conversion of biomass-derived molecules is caused by mass transfer effects, transitions state effects, or external surface catalyzed reactions.

2. Experimental

2.1. Zeolite synthesis

ZSM-5 was synthesized using the organic-free method reported by Kim et al. [38]. A precursor gel of colloidal silica, sodium aluminate, sodium hydroxide, and deionized water was prepared with composition (in terms of molar oxide ratios) of 10 Na_2O:100 SiO_2:3.3 Al_2O_3:3000 H_2O. The precursor was stirred for 2 h at room temperature, and then crystallized under autogenous pressure in a Parr Teflon-lined autoclave at 190 °C for 3 days.

MCM-22 was synthesized using the method reported by Corma et al. [39]. A precursor gel composed of fumed silica, sodium aluminate, sodium hydroxide, distilled water, and hexamethyleneimine (HME) with molar oxide composition of 8.9 Na_2O:100 SiO_2:3.3 Al_2O_3:4500 H_2O:50 HME. The precursor solution stirred for 2 h at room temperature followed by autoclaving at 150 °C for 7 days to crystallize the MCM-22 particles.

TNU-9 and IM-5 were synthesized using previously reported methods [40,41]. The 1,4 bis(N-methyl pyrrolidine) butane (MPB) structure-directing agent was synthesized by the reaction of 1,4 dibromobutane with 1-methyl pyrrolidine in acetone. Similarly, 1,5 bis(N-methyl pyrrolidine) pentane (MPP) was synthesized via reaction of 1,5 dibromopentane with 1-methyl pyrrolidine in acetone. The purity of the products crystallized from this reaction was confirmed by ^1H and ^{13}C NMR performed on a Bruker AV400 spectrometer. Precursor solutions for the TNU-9 particles were prepared with a composition 37 Na_2O:100 SiO_2:2.5 Al_2O_3:4000

H_2O:15 MPB. The IM-5 precursor solution was prepared with a composition of 37 Na_2O:100 SiO_2:2.5 Al_2O_3:4000 H_2O:15 MPP. TNU-9 and IM-5 particles were crystallized by autoclaving their respective precursor solutions for 14 days at 160 °C.

ZSM-11 was synthesized using tetrabutyl ammonium (TBA) as a structure-directing agent [42]. Potassium hydroxide was used in this synthesis to further suppress the formation of ZSM-5 intergrowths [43]. ZSM-11 precursor gels were prepared with molar oxide composition of 6.6 K_2O:3.3 Na_2O:100 SiO_2:3.3 Al_2O_3:4200 H_2O:30 TBA. After stirring for 2 h at room temperature, the precursor gels were autoclaved at 150 °C for 3 days to crystallize the ZSM-11 samples.

SAPO-34 was synthesized following protocols reported in the literature [44]. A precursor solution was prepared using 0.29 g of silica sol (Ludox HS-40, 40 wt.%, Aldrich), 0.36 g of phosphoric acid (85 wt.%, Aldrich), 0.28 g of a hydrated aluminum oxide (a pseudoboehmite, 74.2 wt.% Al_2O_3, 25.8 wt.% H_2O), 0.69 g of triethylamine (TEA) (99.5%, Aldrich), and 1.45 g of water. The composition of the final reaction mixture in molar oxide ratios was 1.0 Al_2O_3:0.8 P_2O_5:1.0 SiO_2:3.5 TEA:50 H_2O. The reaction mixture was crystallized at 180 °C under autogenous pressure for 24 h in the autoclave.

After synthesis, zeolite samples were washed with water and dried at 80 °C. Samples were then calcined in air at 550 °C for 6 h to remove occluded organic molecules. Zeolite samples were ion-exchanged to the H^+ form by treatment in 0.1 M NH_4NO_3 at 70 °C for 24 h followed by filtration, drying at 80 °C overnight, and calcination under air at 550 °C. ZK-5, ZSM-23, SSZ-20, and SSZ-55 samples were supplied by Stacey Zones, Chevron Research and Technology Company, Richmond, California, USA. Ferrierite (CP914C), zeolite Y (CBV 600), and zeolite Beta (CP 814C) were purchased from Zeolyst International, Conshohocken, PA. Physicochemical properties of these zeolites are given in Table 1.

2.2. Characterization

Zeolite structures were confirmed by powder X-ray diffraction as shown in Fig. 2. A Philips X'Pert Pro diffractometer equipped with a X'Celerator detector was used to obtain X-ray patterns. An accelerating voltage of 45 kV was used at 40 mA. Patterns were obtained at a scan rate of 0.1° (2θ) s^{-1}. Powder samples were compacted in an aluminum sample holder with the plane of the powder aligned with the holder surface. The intensity and peak positions of all of the zeolite samples are in good agreement with previously reported spectra [39–41,44,45]. However, TNU-9 shows some impurities and SAPO-34 shows weak peak intensity, indicating that it is less crystalline.

Scanning electron microscopy (SEM) using a JEOL JEM-5400 and JEOL JSM-7400F was employed to characterize the morphology and crystal size of zeolite catalysts. The SEM images of each zeolite catalyst are shown in Fig. 3. ZK-5 and ZSM-23 have spherical crystals of ~0.4 μm while SSZ-20 and SSZ-55 have rod-like crystals of >1 μm. SAPO-34 has a well-defined cubic morphology with a relatively large crystal size of >10 μm. ZSM-5, IM-5, and TNU-9 all have rod-like crystals of <0.5 μm whereas MCM-22 and ZSM-11 have needle-like and rod-like crystal, respectively, with the broad range of crystal size (<1 μm).

Physisorption experiments to characterize the porosity of the zeolites were performed using a Micromeritics ASAP 2010 nitrogen adsorption instrument. All samples were degassed overnight under vacuum at 320 °C before adsorption measurements. Micropore volume was calculated using the t-plot method on the adsorption branch. Mesopore volume was calculated using Barrett–Joyner–Halenda method. Fig. 4 shows N_2 adsorption–desorption isotherms for selected zeolite samples. For MCM-22, IM-5, and TNU-9, significant increase in adsorption in the range $p/p_0 > 0.8$ and hysteresis loops in the desorption branch were observed, indicating the presence of mesopores. Table 2 shows the calculated micropore and mesopore volumes, respectively, for selected zeolite samples. Significant mesopore volumes were observed for MCM-22, IM-5, and TNU-9.

The silica to alumina ratios (SAR) of the zeolites were determined by inductively coupled plasma (ICP) analysis performed by Galbraith Laboratories (Knoxville, TN). Most of the zeolites have the similar silica to alumina ratio between 20 and 50, as shown in Table 1. However, ZSM-23 (SiO_2/Al_2O_3 = 160) and SSZ-20 (SiO_2/Al_2O_3 = 90) were high-silica zeolites while ZK-5 (SiO_2/Al_2O_3 = 5.5) and Y zeolite (SiO_2/Al_2O_3 = 5.2) were high-alumina zeolites.

2.3. Catalytic experiments

Catalytic fast pyrolysis experiments were conducted using a Pyroprobe–GC–MS system (CDS 2000 Analytical Inc.). The probe is a computer-controlled resistively heated element that holds an open-ended quartz tube. Powdered samples (mixtures of glucose and catalyst) are held in the tube with loose quartz wool packing; during pyrolysis vapors flow from the open ends of the quartz tube into a larger cavity (the pyrolysis interface) with a helium carrier gas stream. The carrier gas stream is routed to a model 5890 gas chromatograph (GC) interfaced with a Hewlett Packard model

Table 1
Physico-chemical properties of zeolites used in this study from the International Zeolite Association [45].

Zeolite	IZA code	SiO_2/Al_2O_3	Pore dimension	Ring size (Å)	Pore size (Å)	Internal pore space (Å) [46][b]	CI index
ZK-5	KFI	5.5	3	8	3.9 × 3.9	10.67	>30[c]
SAPO-34	CHA	0.56[a]	3	8	4.3	7.37	33 [47]
Ferrierite	FER	20	2	8, 10	3.5 × 4.8, 4.2 × 5.4	6.31	4.5 [48]
ZSM-23	MTT	160	1	10	4.5 × 5.2	6.19	10.6 [49]
MCM-22	MWW	30	2	10	4.0 × 5.5 4.1 × 5.1	9.69	1.8 [47]
SSZ-20	TON	90	1	10	4.6 × 5.7	5.71	6.9 [49]
ZSM-11	MEL	30	3	10	5.3 × 5.4	7.72	8.7 [50]
ZSM-5	MFI	30	3	10	5.1 × 5.5 5.3 × 5.6	6.36	6.9 [49]
IM-5	IMF	40	3	10	5.5 × 5.6 5.3 × 5.4 5.3 × 5.9	7.34	1.8 [51]
TNU-9	TUN	40	3	10	5.6 × 5.5 5.4 × 5.5	8.46	1.0–2.0[d]
β zeolite	BEA	38	3	12	6.6 × 6.7 5.6 × 5.6	6.68	0.6–2.0 [52]
SSZ-55	ATS	54	1	12	6.5 × 7.25	7.30	1.0–2.0[e]
Y zeolite	FAU	5.2	3	12	7.4 × 7.4	11.24	0.4 [52]

[a] $SiO_2/(Al_2O_3 + P_2O_5)$ in reactant gel.
[b] Maximum included sphere diameter (calculation from packing of the spheres into rigid zeolite frameworks) [46].
[c] Estimated from isomerization of *n*-butene to isobutene [53].
[d] Estimated from isomerization and disproportionation of *m*-xylene [40].
[e] Estimated from isomerization and disproportionation of *m*-xylene [54].

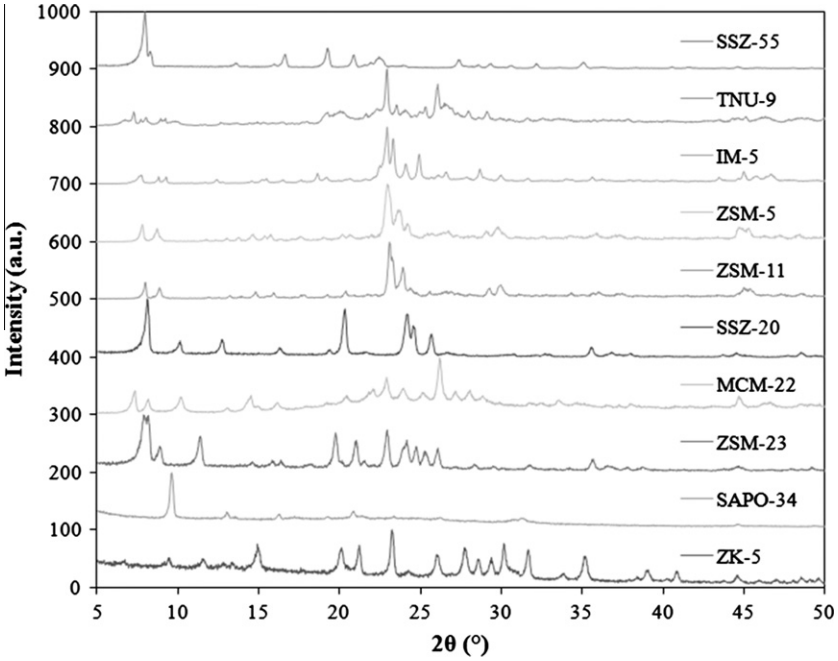

Fig. 2. X-ray diffraction patterns of the zeolites used in this study.

5972A mass spectrometer (MS). The pyrolysis interface was held at 200 °C, and the GC injector temperature was 275 °C. Helium was used as the inert pyrolysis gas as well as the carrier gas for the GC–MS system. A 0.5 mL min^{-1} constant flow program was used for the GC capillary column (Restek Rtx-5sil MS). The GC oven was programmed with the following temperature regime: hold at 45 °C for 4 min, ramp to 250 °C at 10 °C min^{-1}, hold at 250 °C for 15 min. Products were quantified by injecting calibration standards into the GC–MS system. All reactions were carried out under the following conditions: a catalyst-to-feed ratio of 19 (wt/wt), reaction temperature of 600 °C, heating rate of 1000 °C/s, and reaction time of 240 s. We have previously reported that high catalyst-to-feed ratios and fast heating rates are essential to maximize aromatic yields [8]. Prior to the reaction, all catalysts were calcined at 550 °C in air for 5 h. After calcination, powdered samples were prepared by physically mixing the glucose feed and the catalyst. The samples were exposed to ambient air, prior to introduction in the pyroprobe. All yields reported are in molar carbon yield, which is defined as moles of carbon in the products are divided by moles of carbon in the reactants. Carbon on the spent catalyst was quantified by elemental analysis (performed by Galbraith Laboratories using combustion, GLI method # ME-2).

2.4. Determination of kinetic diameter of selected molecules

We define the critical diameter as the diameter of the smallest cylinder inside which the molecule will fit. The maximum diameter is defined as the longest dimension of the molecule. The kinetic diameter (σ) is estimated from the properties of the fluid at the critical point (c), shown in Eqs. (1) and (2) according to Bird et al. [55]:

$$\sigma = 0.841 V_c^{1/3} \quad (1)$$

$$\sigma = 2.44 (T_c/p_c)^{1/3} \quad (2)$$

where V_c is the critical volume in cm^3 mol^{-1}, T_c is the critical temperature in Kelvins and p_c is the critical pressure in atmospheres. Critical point data were obtained from the CRC Handbook [56], Yaws et al. [57], NIST [58] and Wang et al. [59].

The kinetic diameter has also been correlated with the molecular weight using Eq. (3) for aromatic hydrocarbons [59].

$$\sigma = 1.234 (M_W)^{1/3} \quad (3)$$

where M_W is the molecular weight in g mol^{-1}. This kinetic diameter estimation assumes a spherical molecule, and hence the critical mass is related to the size of the sphere [59].

Molecular calculations in this article were performed with Gaussian '03 [60] using density functional theory. Molecule geometries were optimized with the default (eigenvalue-following) optimization algorithm using the B3LYP hybrid functional [61–63] and the 6-31+G(d,p) basis set [64–67] to compute the energy. Critical diameters were computed as the internuclear distance between the two nuclei that intersected the surface of the smallest possible cylinder containing all nuclei plus an estimate of the van der Waals radii of the hydrogen (1.2 Å) or oxygen (1.52 Å) atoms involved. Molecule "lengths" were calculated as the distance between the two farthest-apart atoms along a line orthogonal to the critical diameter, plus an estimate of the atoms' radii.

3. Results and discussion

3.1. Kinetic diameter vs zeolite pore size

We have calculated the critical diameter (width), maximum diameter (length), and kinetic diameter of the biomass feedstocks, oxygenates, and aromatic products from catalytic fast pyrolysis of glucose as shown in Table 3. The data in Table 3 were determined from four sources: the literature, calculation from critical point data using Eqs. (1) and (2), estimation from the molecular weight correlation (Eq. (3)), and molecular calculation. The diameters can differ greatly depending on the source of the information and the calculation used. In general, the common literature values were used. Those calculated using Eqs. (1) and (2) were used when the literature values are not available. Eq. (3) was used when critical point data are not available. Kinetic diameters calculated using

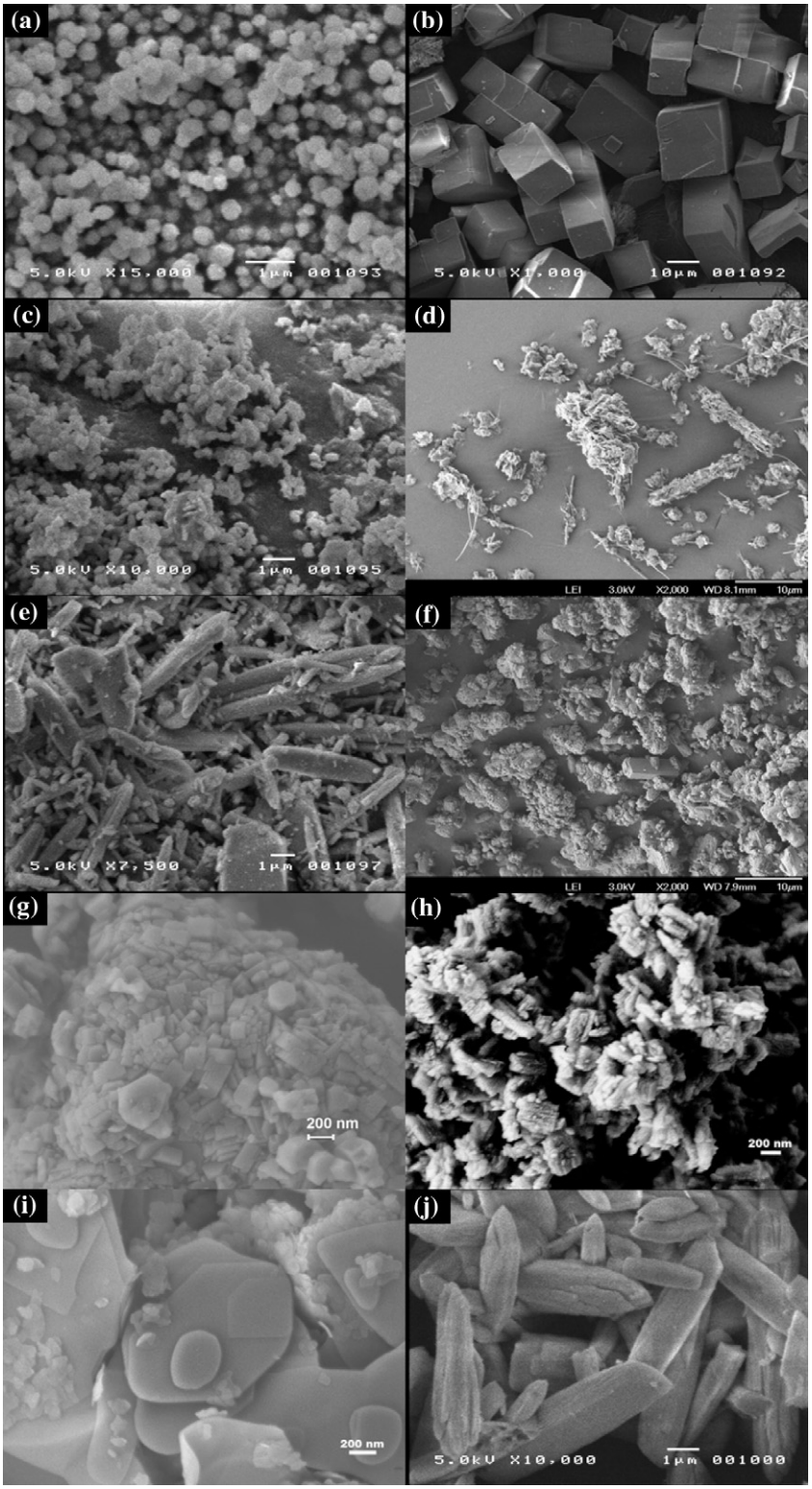

Fig. 3. Scanning electron microscopy images of (a) ZK-5, (b) SAPO-34, (c) ZSM-23, (d) MCM-22, (e) SSZ-20, (f) ZSM-11, (g) ZSM-5, (h) IM-5, (i) TNU-9, and (j) SSZ-55.

the critical volume (Eq. (1)) can differ significantly from Eq. (2). For example, the kinetic diameter for formic acid is either 5.4 Å from critical temperature and pressure data or 4.0 Å using the critical volume. Formic acid forms dimers and this may contribute to the difference [68]. We have used the smaller diameter for the kinetic diameter of the organic acid products for this reason.

The correlation between kinetic diameter and molecular weight is plotted in Fig. 5. The curve from the empirical relationship in Eq. (3) is also plotted in Fig. 5 for comparison to the literature values for oxygenates. In general, there is good agreement (<2% average difference) between the literature values of kinetic diameter and the empirical correlation determined by Wang et al. [59]

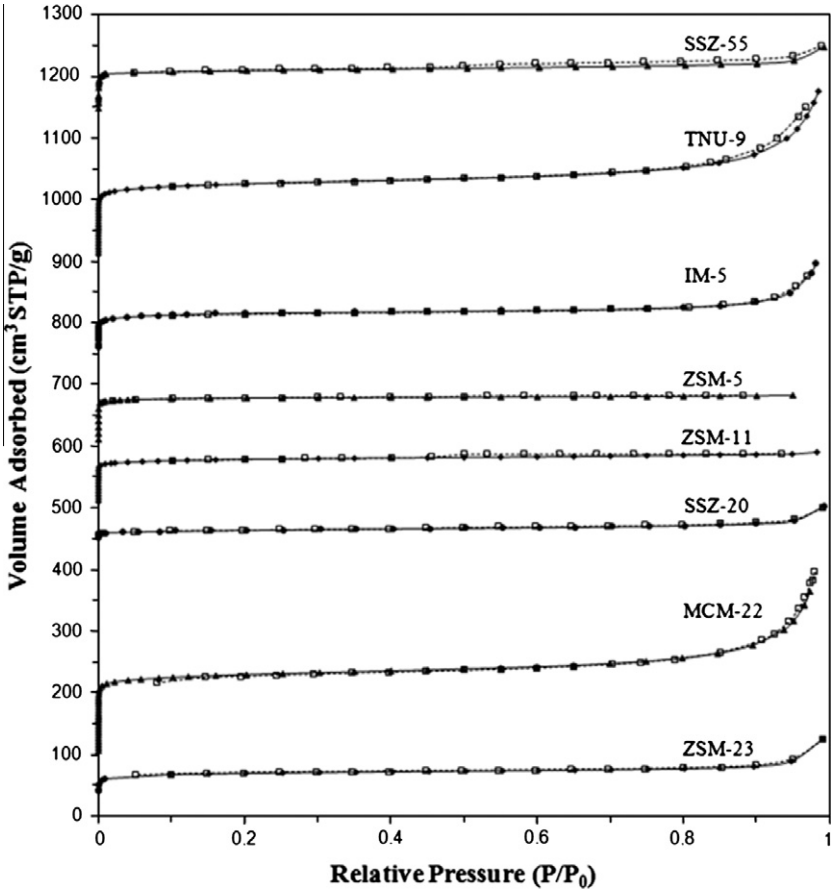

Fig. 4. Nitrogen adsorption–desorption isotherms of selected zeolite catalysts.

Table 2
Micropore and mesopore volumes for the zeolites used in this study.

Zeolite	V_{micro} (cm^3/g)	V_{meso} (cm^3/g)
ZSM-23	0.086	0.09
MCM-22	0.16	0.31
SSZ-20	0.085	0.06
ZSM-11	0.12	0.07
ZSM-5	0.12	0.04
IM-5	0.16	0.15
TNU-9	0.15	0.28
SSZ-55	0.16	0.06

(Eq. (3)), particularly for furan derivatives. This suggests that using this approximation method for the kinetic diameters of oxygenated molecules which do not have critical properties in the literature is reasonable. The molecular weight does not, however, give any indication of the structure of the molecule, and this correlation may differ for different types of structures such as carbohydrates.

The pore sizes of zeolite catalysts are typically given as the crystallographic diameters based on atomic radii, e.g., 5.5–5.6 Å for ZSM-5. Cook and Conner [83] have shown, however, that pore diameters calculated using Norman radii for the Si and O atoms are 0.7 Å larger than those calculated with atomic radii, consistent with the diffusion of molecules of larger diameter than the crystallographic diameter reported, such as cyclohexane diffusion in silicalite. The maximum pore diameters of different zeolites, using atomic radii and the Norman radii corrections, are shown in Table 4.

Fig. 6 shows the kinetic diameters of the feedstock (glucose), the oxygenated products, and aromatic products from catalytic fast pyrolysis of glucose on the same scale as the zeolite pore sizes. The Norman radii adjusted pore sizes are used in this figure to adequately compare the zeolite pore size with the kinetic diameter of the molecules. In the case of zeolites with two different pore sizes, the larger pore sizes were chosen. As shown on this figure, glucose is significantly larger than the maximum pore size of ZSM-5 (6.3 Å); it therefore would not be expected to diffuse into the zeolite before decomposition. However, the decomposition of glucose occurs very rapidly (<1 s) at 600 °C [28] and therefore the diffusion of the pyrolysis products is of more relevance. The pyrolysis products of glucose include levoglucosan, hydroxyacetaldehyde, glyceraldehydes, and furanic compounds. These pyrolysis products, with the exception of levoglucosan, are significantly smaller than the ZSM-5 pore. Levoglucosan can also undergo dehydration reaction to produce products smaller than the pore size of ZSM-5 [84,85]. This suggests that these products can easily diffuse into the zeolite pores and suggests that reactions of these molecules within the ZSM-5 are reactions within the zeolite pores. Inside the ZSM-5 pore, these products are converted into aromatics through a series of dehydration, decarbonylation, decarboxylation, isomerization, oligomerization, and dehydrogenation reactions. It has been reported that the reaction proceeds through a common intermediate or "hydrocarbon pool" composed of these pyrolysis products [86].

Aromatic hydrocarbons are the predominant products along with CO, CO_2, and coke, from the catalytic fast pyrolysis of glucose. From Fig. 6 it can be seen that, benzene, toluene, naphthalene, indene, indane, ethylbenzene, and *p*-xylenes are sufficiently small to diffuse into the ZSM-5 pores. The larger aromatics product molecules including 1,5-dimethylnaphthalene and 1,3,5-trimethyl benzene are most likely formed on the catalyst surface, either directly

Table 3
Dimensions of lignocellulosic feedstocks and products from catalytic pyrolysis.

Molecule	Critical diameter (width) (Å)	Ref.	Maximum diameter (length) (Å)	Ref.	Kinetic diameter, σ (Å)	Ref.
Feedstocks						
α-D-Glucose	8.417	[69]	8.583	[69]	8.6	[70]
β-D-Glucose	8.503	[69]	8.615	[69]	8.6	[70]
Cellulose	~100 (microfibril)	[71]			8.6[a]	
Cellubiose	8.5[a]				8.6[a]	
Xylitol					6.6	Eq. (3)
Oxygenate products (catalyst-to-feed 1.5:1)						
Water	1.89	[58]			3.0, cluster > 6.0	[72]
Carbon monoxide	3.28	[58]	3.339	[58]	3.59	[55]
Carbon dioxide	3.189	[58]	3.339	[58]	3.996	[55]
Acetic acid	3.35	[58]			4.4	[72]
5-Hydroxymethyl furfural (HMF)	5.9	[73]	9.3	[73]	6.2	Eq. (3)
	5.25 trans	Calc.[b]	8.64	Calc.[b]		
	5.48 cis	Calc.[b]	8.64	Calc.[b]		
Formic acid	4.6	[73]	4.6	[73]	4.0	Eq. (1)
Hydroxylacetylaldehyde	3.88	[58]			4.8	Eq. (3)
Furfural	4.56	Calc.[b]	5.99	Calc.[b]	5.5	Eq. (2)
2-Methyl furan					5.3	Eq. (1)
Furan	4.27	[58]			5.1	Eq. (1)
4-Methyl furfural					5.9	Eq. (3)
2-Furanmethanol					5.7	Eq. (3)
Levoglucosan					6.7	Eq. (3)
Hydrocarbon products (catalyst-to-feed 19:1)						
Toluene	6.7	[74]	8.7	[74]	5.85	[75]
Benzene	6.7	[76]	7.4	[76]	5.85	[75]
Indane	6.8[c]				6.3	Eq. (2)
Indene					5.96	[59]
Trimethylbenzene (TMB)	8.35	[76]	8.62	[76]		
1,3,5-TMB	8.178	[77]			8.6	[78]
1,2,4-TMB	7.251	[77]			7.6	[79]
1,2,3-TMB	7.635	[77]			6.6	Eq. (2)
Ethyl benzene	6.7	[74]	9.2	[74]	6.0	[75], Eq. (1)
2-Ethyl toluene					6.6	Eq. (2)
3-Ethyl toluene					6.6	Eq. (2)
4-Ethyl toluene					6.6	Eq. (2)
p-Xylene	6.7	[74]	9.9	[74]	5.85	[75]
m-Xylene	7.4	[74]	9.2	[74]	6.80	[75]
o-Xylene	7.4	[74]	8.7	[74]	6.80	[75]
Naphthalene	6.8	[76]	9.1	[76]	6.2	[59], Eq. (1)
1-Methyl naphthalene	7.65	[80]			6.8	Eq. (2)
1,5-Dimethylnaphthalene					7.7	[81]
1,6-Dimethylnaphthalene					7.7	[81]
2,6-Dimethylnaphthalene					7.2	[81]
Anthracene	6.8	[76]	12.1	[76]	6.96	[59]
Pyrene	7.36	[82]	9.80	[82]	7.24	[59]
Phenanthrene					6.96	[59]

[a] Estimated from glucose.
[b] From Gaussian calculation.
[c] Estimated from naphthalene.

or by processes such as secondary alkylation of the smaller aromatics.

Naphthalene is the aromatic molecule made in the highest yield from catalytic fast pyrolysis of glucose in the pyroprobe reactor [9]. It is known that this polyaromatic hydrocarbon has very slow diffusion in ZSM-5 [9] and it might be speculated that naphthalene is not formed within the pores. Indeed, naphthalene has a kinetic diameter (~6.2 Å [76]) very close to the pore diameter of ZSM-5 (~6.3 Å with Norman radii adjustment [83]). However, at the elevated reaction temperature (600 °C), the energetic barrier to diffusion is likely to be decreased making the zeolites more flexible. Hence, it is possible that naphthalene is formed within the pores as well as on the surface.

Fig. 6 also suggests that zeolites with pore size diameters smaller than 5 Å (8MR ring zeolite, small pore) will predominantly have surface reactions. Larger pore zeolites with pore diameters larger than 7.2 Å (12MR ring zeolite, large pore) will allow all the oxygenates to easily diffuse into the zeolite. These large pore zeolites will primarily have pore reactions.

3.2. Catalytic fast pyrolysis of glucose

The aromatic yield is a strong function of average pore size for the CFP of glucose as shown in Fig. 7. The yield goes through a maximum with the average pore size of the zeolite between 5.3 and 5.5 Å. Small pore zeolites, such as ZK-5 and SAPO-34, produced primarily oxygenated species formed from the pyrolysis of glucose, char, CO, and CO_2. These small pore zeolites are widely used for methanol to olefin conversion [87] and their small pore sizes, 3.9–4.3 Å, do not produce aromatics. Aromatics were produced mainly in the medium pore (10-membered-ring) zeolites, including MCM-22, ZSM-23, SSZ-20, ZSM-11, ZSM-5, IM-5, and TNU-9. All of these zeolites have an effective pore size of 5.2–5.9 Å. Ferrierite (intersecting 8 and 10 ring pore systems) produced primarily oxygenates with low yields of aromatic hydrocarbons. It appears that the 8-membered ring (3.5 × 4.8 Å) pore slows down the overall diffusion rate and inhibits aromatics formation. SSZ-20 and ZSM-23 (one-dimensional pore systems) produced moderate yields of aromatic hydrocarbon with high yields of oxygenates.

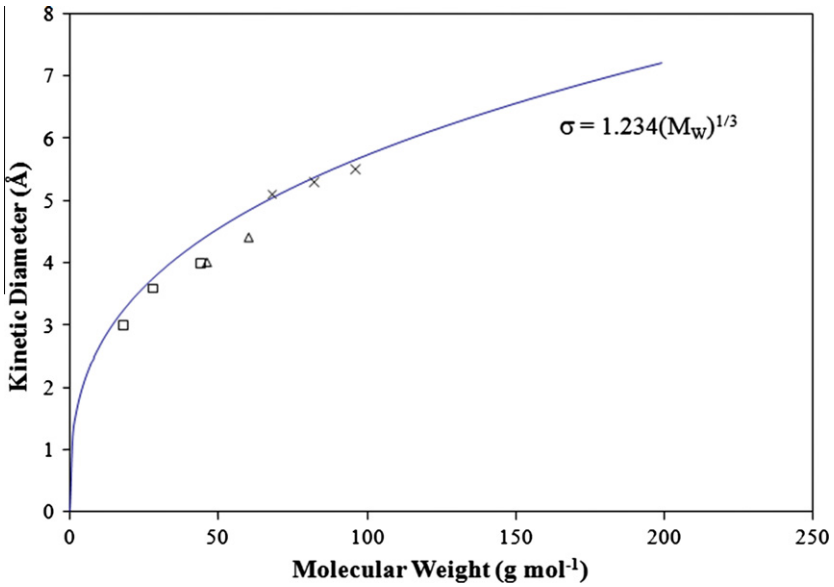

Fig. 5. Correlation between kinetic diameter and molecular weight for oxygenate molecules. □: small molecules; H_2O, CO and CO_2, Δ: organic acids; formic acid and acetic acid, and x: furan derivatives; furan, methyl furan and furfural. The solid curve is a fit using Eq. (3).

Table 4
Maximum pore diameters for different zeolites [45].

Zeolites	Maximum pore diameter (atomic radii) d_A (Å)	Maximum pore diameter (Norman radii) d_N (Å)
SAPO-34	4.3	5.0
MCM-22	5.5	6.2
ZSM-5	5.5 and 5.6	6.2 and 6.3
β zeolite	6.7 and 5.6	7.4 and 6.3
Y zeolite	7.4	8.1

Molecular diffusion inside these one-dimensional pores is more limited than multi-dimensional pores. In addition, these zeolites have high silica to alumina ratio (90 and 160, respectively), which can also impact the catalyst selectivity. Hence, production of the intermediate oxygenate species could be favored. Oxygenates are not produced in the other multi-dimensional 10 ring pore zeolites. Large pore zeolites including Beta zeolite, SSZ-55, and Y zeolite produced aromatics; however, the aromatic yields were low with coke as the major product. Thus, large pores also produce high coke yields.

The maximum aromatic yield of 35% was obtained from ZSM-5, a zeolite with an intersecting 10-membered ring pore system composed of straight (5.3 × 5.6 Å) and sinusoidal (5.1 × 5.5 Å) channels. ZSM-11, formed of two intersecting straight channels (5.3 × 5.4 Å), shows an aromatic yield of 25%. However, MCM-22, TNU-9, and IM-5 show relatively low aromatic yields even though their pore sizes, pore dimensionality, and silica to alumina ratio are similar to ZSM-5 and ZSM-11. As shown in Table 2, these zeolites have high mesopore volumes created by inter-crystalline spaces, compared to ZSM-5 and ZSM-11. This suggests that these mesopores act as large pores, facilitating the formation of coke.

Further insights into the differences in the reactivity of medium pore zeolites can be obtained from the size of internal pore space (i.e., pore intersections). As shown in Table 1, MCM-22 and

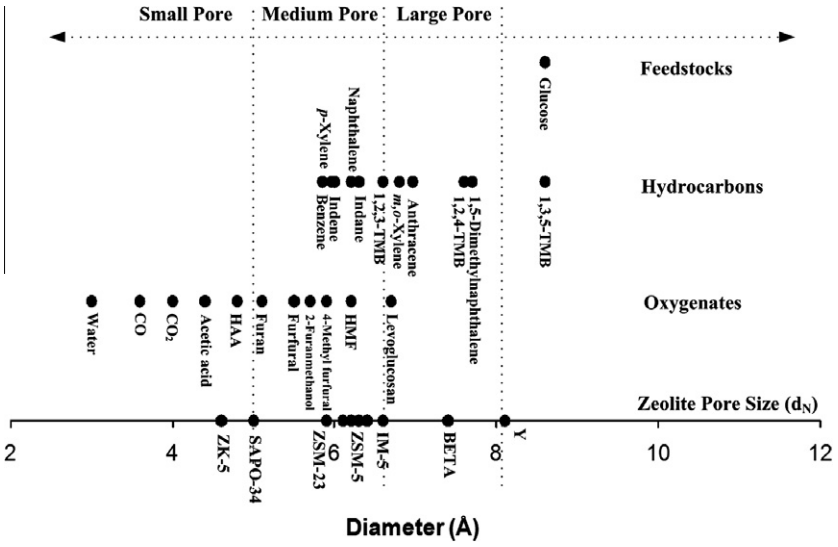

Fig. 6. Schematic of zeolite pore diameter (d_N) compared to the kinetic diameter of feedstocks, and oxygenate and hydrocarbon catalytic pyrolysis products.

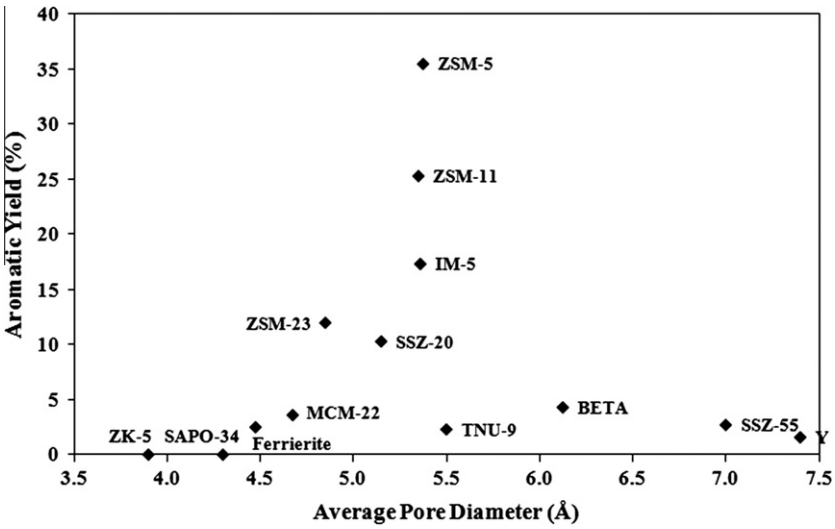

Fig. 7. Aromatic yields as a function of average pore diameter for different zeolites for catalytic fast pyrolysis of glucose. Reaction conditions: catalyst-to-feed weight ratio = 19, nominal heating rate 1000 °C s^{-1}, reaction time 240 s.

TNU-9 have large internal pore spaces of 9.69 Å and 8.46 Å, respectively, compared to that of ZSM-5 (6.36 Å) and ZSM-11 (7.72 Å). Thus, these results suggest that, in addition to pore window size, the steric hindrance of reacting molecules inside zeolite pores plays a role in this reaction. This also suggests that biomass conversion into aromatics with zeolites is a reaction where there are both mass transfer and transition state effects within the zeolite.

Table 5 shows the carbon yield of these reactions. Tables 6 and 7 show the product distributions of aromatics and oxygenated species, respectively. The major glucose pyrolysis product is levoglucosan (LGA, 1,6-anhydro-β-D-glucopyranose, $C_6H_{10}O_5$), which is the dehydrated product of glucose [28]. Other anhydrosugars, including levoglucosenone (LGO, 6,8-dioxabicyclo[3.2.1]oct-2-en-4-one, $C_6H_6O_3$), 1,4:3,6-dianhydro-β-D-glucopyranose (DGP, $C_6H_8O_4$), and 1,6-anhydro-β-d-glucofuranose (AGF, $C_6H_{10}O_5$), are present in lower amounts. However, as shown in Table 7, levoglucosenone and furfural become the major products among the produced oxygenate species for ZK-5 and SAPO-34. This suggests that levoglucosan is further dehydrated by surface catalyzed reaction because these small pore zeolites do not allow any oxygenate species to diffuse into the pore. Moreover, levoglucosan was only dominant for ZSM-23 (SiO_2/Al_2O_3 = 160), the high-silica catalyst. In ZSM-23, the surface acid sites have relatively low concentration, and this could minimize the surface catalyzed reaction. Hence, this oxygenate distribution combined with the kinetic diameter estimation clearly shows the role of surface reaction in catalytic fast pyrolysis of glucose.

The gaseous products are CO and CO_2 for all the catalysts, as shown in Table 5. These gaseous product yields increased with increasing aromatic yield. In order to produce aromatics, oxygen for the intermediate pyrolysis products has to be removed by CO, CO_2, and water. Hence, the small pore zeolite (no aromatic production) produced relatively low CO and CO_2 yield compared to medium pore and large pore zeolites. Especially, CO and CO_2 yields are remarkably high for IM-5, ZSM-11, and ZSM-5 which produce high aromatic yield.

As shown in Table 6, the major aromatic products are naphthalenes(N), toluene(T), xylenes(X), and benzene(B) for all of the catalysts. The aromatic distribution was a function of zeolite type. However, aromatic distribution was not a simple function of zeolite pore. For one-dimensional zeolites such as ZSM-23, SSZ-20, and SSZ-55, naphthalene selectivity increased with increasing the pore size of zeolite (24.9%, 38.3%, and 47.2%). On the other hand, the opposite trend was observed for 2 and 3 dimensional zeolites. Large pore zeolites such as Beta and Y zeolite showed relatively low naphthalene selectivity and high BTX selectivity compared to medium pore zeolites even though their large pores can facilitate the production of larger aromatic molecules. Interestingly, aromatic distribution of medium pore TNU-9 was similar to large pore zeolites. This aromatic distribution results suggest that the internal

Table 5
Carbon yields (%) for catalytic fast pyrolysis of glucose with different zeolites. Reaction conditions: catalyst-to-feed weight ratio = 19, nominal heating rate 1000 °C s^{-1}, reaction time 240 s.

Zeolite	Aromatics	Oxygenates	CO_2	CO	Coke	Unidentified[a]	Total carbon
ZK-5	0.0	14.1	4.3	8.7	55.1	17.8	100.0
SAPO-34	0.0	30.0	3.2	7.7	34.7	24.4	100.0
Ferrierite	2.5	14.1	4.4	11.6	48.0	19.4	100.0
ZSM-23	12.0	12.7	4.8	10.5	40.8	19.2	100.0
MCM-22	3.6	0	10	26	63	–	102
SSZ-20	10.3	18.0	4.1	9.7	43.1	14.8	100.0
ZSM-11	25.3	0	11.0	24.9	44.7	–	106
ZSM-5	35.5	0	8.9	23.3	30.4	–	98.1
IM-5	17.3	0	10	28	48.5	–	103.8
TNU-9	2.3	0	5.6	15.9	66.8	9.4	90.6
β zeolite	4.3	<1	10.5	7.8	67.0	10.4	89.6
SSZ-55	2.7	<1	3.7	14.1	83.7	–	104.2
Y zeolite	1.6	<1	3.9	13.4	84.9	–	103.8

[a] Unidentified includes unidentified oxygenate species in GC–MS and missing carbon.

Table 6
Aromatic product selectivity for catalytic fast pyrolysis of glucose with different zeolites. Reaction conditions: catalyst-to-feed weight ratio 19, nominal heating rate 1000 °C s^{-1}, reaction time 240 s. Abbreviations: Ben. = benzene, Tol. = toluene, E-Ben. = ethyl-benzene, Xyl. = xylenes, M,E-Ben. = methyl-ethyl-benzene, Tm-Ben. = trimethylbenzene, Ph. = phenols, Ind. = indanes, Nap. = naphthalenes. Others include ethyl-dimethyl-benzene and methyl-propenyl-benzene.

Catalyst	Aromatic selectivity (%)							
	Ben.	Tol.	E-Ben. Xyl.	M,E-Benz. Tm-Benz.	Ph.	Ind.	Naph.	Others
ZK-5	–	–	–	–	–	–	–	–
SAPO-34	–	–	–	–	–	–	–	–
Ferrierite	3.1	18.4	8.2	0.0	14.2	4.6	51.6	0.0
ZSM-23	10.6	25.8	19.3	6.2	3.8	6.9	24.9	2.4
MCM-22	29.4	25.2	10.2	0.0	0.0	0.0	35.1	0.0
SSZ-20	7.3	23.1	16.8	5.4	1.3	8.0	38.3	0.0
ZSM -11	14.2	27.1	17.3	1.5	2.5	4.4	32.6	0.4
ZSM-5	12.8	18.5	12.9	2.6	0.1	2.2	50.7	0.3
IM-5	17.4	25.4	11.4	3.2	0.4	0.7	41.5	0.0
TNU-9	31.9	40.0	11.1	0.0	0.0	0.0	16.9	0.0
β zeolite	30.9	34.7	13.4	0.9	0.0	0.0	20.1	0.0
SSZ-55	13.3	27.9	9.1	1.2	1.3	0.0	47.2	0.0
Y zeolite	20.6	31.0	12.5	1.6	5.3	0.0	29.1	0.0

Table 7
Oxygenated product selectivity for catalytic fast pyrolysis of glucose with different zeolites. Reaction conditions: catalyst-to-feed weight ratio 19, nominal heating rate 1000 °C s^{-1}, reaction time 240 s.

Oxygenate selectivity (%)	Catalyst				
	ZK-5	SAPO-34	Ferrierite	ZSM-23	SSZ-20
Acetic acid	0.0	1.5	0.0	20.4	8.1
4-Methyl-2,3-dihydrofuran	10.1	12.3	9.6	8.5	12.3
Furfural	40.0	23.7	30.6	5.0	13.1
5-Methyl furfural	3.0	4.1	2.0	0.0	0.0
2-Furanmethanol	1.7	2.8	1.4	0.9	1.9
Furancarboxylic acid, methyl ester	1.6	2.6	1.1	0.0	2.5
5-Methyl-2(5H)-furanone	0.6	0.7	0.8	0.0	1.0
5-Hydroxymethyl furfural	1.5	11.5	0.0	0.0	0.0
Isomaltol	0.7	1.3	0.0	0.0	0.7
Ethanone, 1-(2-furanyl)-	1.2	1.6	0.0	0.0	0.0
2-Hydroxymethylene-tetrahydrofuran-3-one	2.5	2.8	1.1	0.0	3.0
1,4:3,6-Dianhydro-alpha-D-glucopyranose	5.8	12.6	10.1	9.0	8.9
1,6-Anhydro-beta-D-glucopyranose (Levoglucosan)	5.0	0.0	0.0	22.9	0.0
Levoglucosenone	26.3	22.5	43.2	33.7	48.4

pore architecture of zeolite plays a significant role on the reaction chemistry.

3.3. Aromatic yields as a function of constraint index

The constraint index (CI) is a widely used concept to investigate the shape selectivity of zeolites [88]. It is defined as the ratio of the observed cracking rate constants of n-hexane to 3-methylpentane; a higher CI value thus indicates a larger steric hindrance and a lower CI value indicates the absence of steric hindrance. Fig. 8 shows the aromatic yield as a function of constraint index. It was found that the medium pore zeolites with moderate CI values produce high aromatic yield. IM-5 and TNU-9 have low CI values of 1.8 and 1.0–2.0 compared to the 6.9 of ZSM-5. Hence, a low CI index

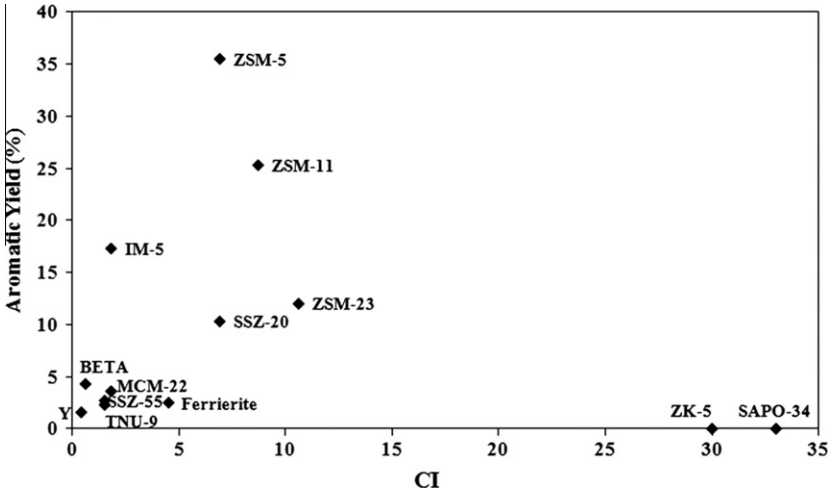

Fig. 8. Aromatic yields versus the constraint index.

(less steric hindrance) is not preferable for aromatic formation. Notably, ZSM-23 and SSZ-20, CI values of 10.6 and 6.9, respectively, show higher aromatic yields than the zeolites with low CI values (except IM-5). It is also remarkable that TNU-9 and MCM-22 produced significant amounts of coke (66.8% and 63%) along with aromatics, behaving like large pore zeolites. This can be explained by the presence of the cages inside the zeolite pores (i.e., the effect of pore intersections). MCM-22 and TNU-9 have large cylindrical pore intersections (7.1 Å) and large cavities accessible through 10 ring pore window, respectively [40]. Thus, we believe that these cages inside the zeolite channels can provide the space needed for coke formation. Carpenter et al. [89] also showed that the presence of a large cage can contribute to the low CI values and fast deactivation of the zeolite by providing more void space.

3.4. Design of zeolite catalysts for conversion of biomass-derived oxygenates into aromatics

The results in this paper can be used to design new zeolite catalyst for the conversion of biomass-derived oxygenates into aromatics. The reaction for the conversion of biomass-derived molecules into aromatics is a shape selective reaction where the shape selectivity effect is caused by both mass transfer effects, linked to the pore window size of zeolite, and transition state effects, related to the internal void space of zeolites. The external surface acid sites also contribute to the dehydration of pyrolysis products to smaller oxygentates and production of larger aromatic molecules which are less valuable products. Based on our results, ZSM-5 is the optimal zeolite structure having the ideal pore size and internal pore space for biomass conversion. ZSM-5 can be further modified to improve its catalytic properties. The mass transfer effects can be varied by changing the crystallite size of ZSM-5. Small crystallite size of ZSM-5 might be beneficial by enhancing diffusion of molecules within the catalyst and creating high surface area for access of molecules into acid sites [90]. Alternatively, recent advances in hierarchical zeolite synthesis allows us to introduce mesoporosity into ZSM-5 framework [91–94]. Carefully designed mesoporous ZSM-5 might have benefits of enhanced mass transfer and transformation of bulky molecules through the mesoporosity. It has been reported that the mesoporous ZSM-5 exhibited the enhanced catalytic activity for upgrading of pyrolysis vapors to aromatics [95,96]. Transition state effect can be adjusted by incorporating different types of sites preferentially within the ZSM-5. These sites located inside ZSM-5 pores can provide new active sites for reaction (e.g. hydrogenation) and enhanced steric hindrance. In addition, the surface acid sites of ZSM-5 can be tuned to decrease the secondary reaction on the catalyst surface. Decreasing the exterior surface acidity by dealumination or silylating agent treatment might reduce the formation of the undesired larger aromatic molecules. As suggested in this paper, the catalytic properties of ZSM-5 can be optimized in many ways. Proper tuning of each parameter can offer highly selective zeolite catalysts for the conversion of biomass-derived oxygenates into aromatics.

4. Conclusions

We studied the influence of zeolite pore size and shape selectivity on the conversion of glucose to aromatics by catalytic fast pyrolysis. We first estimated the kinetic diameters for the reactants and products to determine whether the reactions occur inside the pores or at external surface sites for the different zeolite catalysts. This analysis showed that the majority of the aromatic products and the reactants can fit inside the zeolite pores of most of the medium and large pore zeolites. However, in some of the smaller pore zeolites, the polycyclic aromatics may form by secondary reactions on the catalyst surface, either directly or via reaction of the smaller aromatics. Zeolites having a wide range of pore size and shape (small pore ZK-5, SAPO-34, medium pore Ferrierite, ZSM-23, MCM-22, SSZ-20, ZSM-11, ZSM-5, IM-5, TNU-9, and large pore SSZ-55, Beta zeolite, Y zeolite) were tested in a pyroprobe reactor for the conversion of glucose to aromatics. The aromatic yield was a function of the pore size of the zeolite catalyst. Small pore zeolites did not produce any aromatics with oxygenated products (from pyrolysis of glucose), CO, CO_2 and coke as the major products. Aromatic yields were highest in the medium pore zeolites with pore sizes in the range of 5.2–5.9 Å. High coke yield, low aromatic yields, and low oxygenate yields were observed with large pore zeolites, suggesting that the large pores facilitate the formation of coke. In addition to pore window size, internal pore space and steric hindrance play a determining role for aromatic production. Medium pore zeolites with moderate internal pore space and steric hindrance (ZSM-5 and ZSM-11) have the highest aromatic yield and the least amount of coke.

Acknowledgments

This work was supported by a National Science Foundation CAREER award (Grant #747996) and by the Defense Advanced Research Project Agency through the Defense Science Office Cooperative Agreement W911NF-09-2-0010 (Surf-Cat: Catalysts for production of JP-8 range molecules from lignocellulosic Biomass. Approved for Public Release, Distribution Unlimited). The views, opinions, and/or findings contained in this article are those of the author and should not be interpreted as representing the official views or policies, either expressed or implied, of the Defense Advanced Research Projects Agency or the Department of Defense.

References

[1] G.W. Huber, S. Iborra, A. Corma, Chem. Rev. 106 (2006) 4044.
[2] A.V. Bridgwater, Chem. Eng. J. 91 (2003) 87.
[3] D. Mohan, C.U. Pittman Jr., P.H. Steele, Energy Fuels 20 (2006) 848.
[4] A. Pattiya, J.O. Titiloye, A.V. Bridgwater, J. Anal. Appl. Pyrolysis 81 (2008) 72.
[5] A. Pattiya, J.O. Titiloye, A.V. Bridgwater, Fuel 89 (2010) 244.
[6] A. Aho, N. Kumar, K. Eranen, T. Salmi, M. Hupa, D.Y. Murzin, Fuel 87 (2008) 2493.
[7] A. Corma, G.W. Huber, L. Sauvanaud, P. O'Connor, J. Catal. 247 (2007) 307.
[8] T.R. Carlson, T.P. Vispute, G.W. Huber, ChemSusChem 1 (2008) 397.
[9] T.R. Carlson, G.A. Tompsett, W.C. Conner, G.W. Huber, Top. Catal. 52 (2009) 241.
[10] R. French, S. Czernik, Fuel Process. Technol. 91 (2010) 25.
[11] M. Olazar, R. Aguado, J. Bilbao, A. Barona, Aiche J. 46 (2000) 1025.
[12] P.T. Williams, P.A. Horne, J. Anal. Appl. Pyrolysis 31 (1995) 39.
[13] R.K. Sharma, N.N. Bakhshi, Energy Fuels 7 (1993) 306.
[14] S.P.R. Katikaneni, J.D. Adjaye, N.N. Bakhshi, Energy Fuels 9 (1995) 1065.
[15] B. Valle, A.G. Gayubo, A.T. Aguayo, M. Olazar, J. Bilbao, Energy Fuels 24 (2010) 2060.
[16] N.Y. Chen, T.F. Degnan Jr., L.R. Koenig, Chemtech 16 (1986) 506.
[17] P.T. Williams, P.A. Horne, Fuel 74 (1995) 1839.
[18] P.T. Williams, P.A. Horne, J. Inst. Energy 69 (1996) 176.
[19] J. Adam, E. Antonakou, A. Lappas, M. Stocker, M.H. Nilsen, A. Bouzga, J.E. Hustad, G. Oye, Micropor. Mesopor. Mater. 96 (2006) 93.
[20] S. Vitolo, B. Bresci, M. Seggiani, M.G. Gallo, Fuel 80 (2000) 17.
[21] J.D. Adjaye, N.N. Bakhshi, Biomass Bioenergy 7 (1994) 201.
[22] J.D. Adjaye, N.N. Bakhshi, Fuel Process. Technol. 45 (1995) 161.
[23] A.A. Boateng, C.A. Mullen, C.M. McMahan, M.C. Whalen, K. Cornish, J. Anal. Appl. Pyrolysis 87 (2010) 14.
[24] H.Y. Zhang, R. Xiao, H. Huang, G. Xiao, Bioresour. Technol. 100 (2009) 1428.
[25] P.T. Williams, N. Nugranad, Energy 25 (2000) 493.
[26] A. Ausavasukhi, T. Sooknoi, D.E. Resasco, J. Catal. 268 (2009) 68.
[27] T.Q. Hoang, X.L. Zhu, T. Danuthai, L.L. Lobban, D.E. Resasco, R.G. Mallinson, Energy Fuels 24 (2010) 3804.
[28] T.R. Carlson, J. Jae, Y.C. Lin, G.A. Tompsett, G.W. Huber, J. Catal. 270 (2010) 110.
[29] P.B. Weisz, Pure Appl. Chem. 52 (1980) 2091.
[30] B. Smit, T.L.M. Maesen, Chem. Rev. 108 (2008) 4125.
[31] S.M. Csicsery, Zeolites 4 (1984) 202.
[32] S.M. Csicsery, Chem. Br. 21 (1985) 473.
[33] J.C. Cheng, T.F. Degnan, J.S. Beck, Y.Y. Huang, M. Kalyanaraman, J.A. Kowalski, C.A. Loehr, D.N. Mazzone, in: H. Hattori, K. Otsuka (Eds.), A Comparison of Zeolites MCM-22, beta, and USY for Liquid Phase Alkylation of Benzene with Ethylene, Science and Technology in Catalysis 1998, Elsevier Science Publ. B.V., Amsterdam, 1999, p. 53.

[34] G. Sastre, C.R.A. Catlow, A. Corma, J. Phys. Chem. B 103 (1999) 5187.
[35] E.G. Derouane, J.B. Nagy, C. Fernandez, Z. Gabelica, E. Laurent, P. Maljean, Appl. Catal. 40 (1988) L1.
[36] E.G. Derouane, J.B. Nagy, Appl. Catal. 52 (1989) 169.
[37] E.G. Derouane, J. Mol. Catal. A – Chem. 134 (1998) 29.
[38] S.D. Kim, S.H. Noh, K.H. Seong, W.J. Kim, Micropor. Mesopor. Mater. 72 (2004) 185.
[39] A. Corma, C. Corell, J. Perezpariente, Zeolites 15 (1995) 2.
[40] S.B. Hong, H.K. Min, C.H. Shin, P.A. Cox, S.J. Warrender, P.A. Wright, J. Am. Chem. Soc. 129 (2007) 10870.
[41] S.H. Lee, D.K. Lee, C.H. Shin, Y.K. Park, P.A. Wright, W.M. Lee, S.B. Hong, J. Catal. 215 (2003) 151.
[42] G. Gonzalez, M.E. Gomes, G. Vitale, G.R. Castro, Micropor. Mesopor. Mater. 121 (2009) 26.
[43] G.A. Jablonski, L.B. Sand, J.A. Gard, Zeolites 6 (1986) 396.
[44] S.H. Jhung, J.S. Chang, J.S. Hwang, S.E. Park, Micropor. Mesopor. Mater. 64 (2003) 33.
[45] http://www.iza-online.org.
[46] M.M.J. Treacy, M.D. Foster, Micropor. Mesopor. Mater. 118 (2009) 106.
[47] Z.R. Zhu, Q.L. Chen, Z.K. Xie, W.M. Yang, C. Li, Micropor. Mesopor. Mater. 88 (2006) 16.
[48] M.D. Macedonia, E.J. Maginn, Aiche J. 46 (2000) 2504.
[49] S.I. Zones, T.V. Harris, Micropor. Mesopor. Mater. 35–6 (2000) 31.
[50] N.Y. Chen, W.E. Garwood, J. Catal. 52 (1978) 453.
[51] S.I. Zones, C.Y. Chen, A. Corma, M.T. Cheng, C.L. Kibby, I.Y. Chan, A.W. Burton, J. Catal. 250 (2007) 41.
[52] Y.F. Chu, US Patent, 4 927 525, 1990.
[53] J. Houzvicka, S. Hansildaar, V. Ponec, J. Catal. 167 (1997) 273.
[54] M.D.S. Machado, J. Perez-Pariente, E. Sastre, D. Cardoso, M.V. Giotto, J.L. Garcia-Fierro, V. Fornes, J. Catal. 205 (2002) 299.
[55] R.B. Bird, W.E. Stewart, E.N. Lightfoot, Transport Phenomena, John Wiley & Sons, New York, 1960. p. 26.
[56] D.R. Lide, CRC Handbook of Chemistry and Physics, CRC, 2008.
[57] C.L. Yaws, Chemical Properties Handbook, McGraw Hill, New York, 1999.
[58] Computational Chemistry Database, NIST, 2008. <http://cccbdb.nist.gov/>.
[59] H. Wang, M. Frenklach, Combust. Flame 96 (1994) 163.
[60] M.J. Frisch, G.W. Trucks, H.B. Schlegel, G.E. Scuseria, M.A. Robb, J.R. Cheeseman, J.J.A. Montgomery, T. Vreven, K.N. Kudin, J.C. Burant, J.M. Millam, S.S. Iyengar, J. Tomasi, V. Barone, B. Mennucci, M. Cossi, G. Scalmani, N. Rega, G.A. Petersson, H. Nakatsuji, M. Hada, M. Ehara, K. Toyota, R. Fukuda, J. Hasegawa, T. Nakajima, Y. Honda, O. Kitao, H. Nakai, M. Klene, X. Li, J.E. Knox, H.P. Hratchian, J.B. Cross, V. Bakken, C. Adamo, J. Jaramillo, R. Gomperts, R.E. Stratmann, O. Yazyev, A.J. Austin, R. Cammi, C. Pomelli, J.W. Ochterski, P.Y. Ayala, K. Morokuma, G.A. Voth, P. Salvador, J.J. Dannenberg, V.G. Zakrzewski, S. Dapprich, A.D. Daniels, M.C. Strain, O. Farkas, D.K. Malick, A.D. Rabuck, K. Raghavachari, J.B. Foresman, J.V. Ortiz, Q. Cui, A.G. Baboul, S. Clifford, J. Cioslowski, B.B. Stefanov, G. Liu, A. Liashenko, P. Piskorz, I. Komaromi, R.L. Martin, D.J. Fox, T. Keith, M.A. Al-Laham, C.Y. Peng, A. Nanayakkara, M. Challacombe, P.M.W. Gill, B. Johnson, W. Chen, M.W. Wong, C. Gonzalez, J.A. Pople, Gaussian '03, Gaussian, Inc., Wallingford, CT, 2003.
[61] A.D. Becke, J. Chem. Phys. 98 (1993) 5648.
[62] C.T. Lee, W.T. Yang, R.G. Parr, Phys. Rev. B 37 (1988) 785.
[63] P.J. Stephens, F.J. Devin, C.F. Chabalowski, M.J. Frisch, J. Phys. Chem. 98 (1994) 11623.
[64] W.J. Hehre, R. Ditchfield, J.A. Pople, J. Chem. Phys. 56 (1972) 2257.
[65] P.C. Hariharan, J.A. Pople, Theoret. Chim. Acta (Berl.) 28 (1973) 213.
[66] P.C. Hariharan, J.A. Pople, Mol. Phys. 27 (1974) 209.
[67] M.M. Francl, W.J. Pietro, W.J. Hehre, J.S. Binkley, M.S. Gordon, D.J. DeFrees, J.A. Pople, J. Chem. Phys. 77 (1982) 3654.
[68] M. Krossner, J. Sauer, J. Phys. Chem. 100 (1996) 6199.
[69] R. Netrabukkana, K. Lourvanij, G.L. Rorrer, Ind. Eng. Chem. Res. 35 (1996) 458.
[70] S. Li, V.A. Tuan, J.L. Falconer, R.D. Noble, J. Membr. Sci. 191 (2001) 53.
[71] D. Topgaard, O. Soederman, Langmuir 17 (2001) 2694.
[72] T.C. Bowen, Richard D. Noble, J.L. Falconer, J. Membr. Sci. 245 (2004) 1.
[73] K. Lourvanij, G.L. Rorrer, J. Chem. Technol. Biotechnol. 69 (1997) 35.
[74] V.R. Choudhary, Vikram S. Nayak, T.V. Choudhary, Ind. Eng. Chem. Res. 36 (1997) 1812.
[75] C.D. Baertsch, H.H. Funke, J.L. Falconer, R.D. Noble, J. Phys. Chem. 100 (1996) 7676.
[76] D.M. Ruthven, B.K. Kaul, Ind. Eng. Chem. Res. 32 (1993) 2053.
[77] C.E. Webster, R.S. Drago, M.C. Zerner, J. Phys. Chem. B 103 (1999) 1242.
[78] J. Cejka, J. Kotrla, A. Krejci, Appl. Catal. A – Gen. 277 (2004) 191.
[79] N.M. Tukur, S. Al-Khattaf, Energy Fuels 21 (2007) 2499.
[80] R.M. Moore, J.R. Katzer, Aiche J. 18 (1972) 816.
[81] N. Kraikul, P. Rangsunvigit, S. Kulprathipanja, Adsorption 12 (2006) 317.
[82] E.H. Ellison, J. Phys. Chem. B 103 (1999) 9314.
[83] M. Cook, W.C. Conner, How big are the pores of zeolites?, in: Proceedings of the International Zeolite Conference, 12th, July 5–10, 1998, Baltimore, 1999, p. 409.
[84] Y.C. Lin, J. Cho, G.A. Tompsett, P.R. Westmoreland, G.W. Huber, J. Phys. Chem. C 113 (2009) 20097.
[85] H. Kawamoto, M. Murayama, S. Saka, J. Wood Sci. 49 (2003) 469.
[86] T.R. Carlson, J. Jae, G.W. Huber, ChemCatChem 1 (2009) 107.
[87] M. Stocker, Micropor. Mesopor. Mater. 29 (1999) 3.
[88] V.J. Frillette, W.O. Haag, R.M. Lago, J. Catal. 67 (1981) 218.
[89] J.R. Carpenter, S. Yeh, S.I. Zones, M.E. Davis, J. Catal. 269 (2010) 64.
[90] T.Q. Hoang, X.L. Zhu, L.L. Lobban, D.E. Resasco, R.G. Mallinson, Catal. Commun. 11 (2010) 977.
[91] W. Fan, M.A. Snyder, S. Kumar, P.S. Lee, W.C. Yoo, A.V. McCormick, R.L. Penn, A. Stein, M. Tsapatsis, Nat. Mater. 7 (2008) 984.
[92] M. Hartmann, Angew. Chem. Int. Ed. 43 (2004) 5880.
[93] J. Perez-Ramirez, C.H. Christensen, K. Egeblad, J.C. Groen, Chem. Soc. Rev. 37 (2008) 2530.
[94] M. Choi, K. Na, J. Kim, Y. Sakamoto, O. Terasaki, R. Ryoo, Nature 461 (2009) 246.
[95] H.J. Park, H.S. Heo, J.K. Jeon, J. Kim, R. Ryoo, K.E. Jeong, Y.K. Park, Appl. Catal. B – Environ. 95 (2010) 365.
[96] K.H. Park, H.J. Park, J. Kim, R. Ryoo, J.K. Jeon, J. Park, Y.K. Park, J. Nanosci. Nanotechnol. 10 (2010) 355.